

Broadband Antireflection Coatings Employing Multiresonant Dielectric Metasurfaces

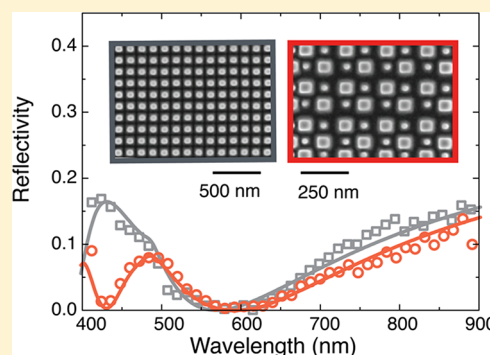
Emanuele F. Pecora,[†] Andrea Cordaro,[†] Pieter G. Kik,^{†,‡} and Mark L. Brongersma^{*,†}

[†]Geballe Laboratory for Advanced Materials, Stanford University, Stanford, California 94305, United States

[‡]CREOL, The College of Optics and Photonics, University of Central Florida, 4000 Central Florida Blvd, Orlando, Florida 32816, United States

ABSTRACT: The energy efficiency of optoelectronic components and devices is critically dependent on minimizing undesired reflections from interfaces between materials with differing optical properties. Antireflection coatings based on metamaterials with deep-subwavelength features offer superior performance over their homogeneous counterparts as they afford subtle tuning of the refractive index and gradients therein. Recent work also showed that arrays of larger-sized (250 nm diameter), high-index nanostructures placed on semiconductor surfaces reduce the reflectivity by capitalizing on optical Mie resonances. Here, we start by demonstrating that a judiciously designed, single Mie resonator can enable perfect, local antireflection at its resonance frequency. This insight opens the door to the development of entirely new, multiresonant antireflection coating (ARC) designs in which differently sized Mie resonators manage antireflection at different wavelengths. We demonstrate the value of such multiresonant ARCs for solar applications by showing an average reflectivity as low as 4% from a silicon wafer across the visible range.

KEYWORDS: metamaterials, nanowires, antireflection coating, optical resonators, silicon



The reduction of unwanted reflections at interfaces has been a longstanding challenge, and starting with the pioneering work by Raleigh,¹ the design of ARCs has seen tremendous developments. The rapid expansion of the solar, display, touchscreen, imaging, and augmented reality markets has further increased the need and required a level of sophistication of these specialty optical coatings. Ideal ARCs are broadband, insensitive to incident angle, robust, and allow for low-cost, facile device integration. To achieve such high performance, the simple quarter-wavelength ARCs made from nonabsorbing, homogeneous materials have evolved into complex nanostructured coatings.^{2–9} By structuring layers at a scale that is well below the illumination wavelength, one can tailor their effective optical properties to realize gradient index ARCs or metamaterial films mimicking conventional quarter-wavelength or multilayered ARCs.^{10–17} The widespread adoption of such complex layers in commercial applications has been limited by their fabrication cost as well as mechanical adhesion and stability of the various layers. In an alternative approach, the scattering properties of optically resonant metallic and dielectric^{18–22} antennas have also been harnessed to reduce reflection from interfaces. Arrays of these larger structures (~100 nm) can quite easily be realized in a single patterning step by a number of nanofabrication approaches. Armed with newly emerging insights into the operation of high-index semiconductor Mie resonators and metamaterials,²³ we demonstrate a conceptually new multiresonant antire-

flection coating design that offers superior broadband antireflection.

In a pioneering experimental work,¹⁹ Polman and co-workers showed that the placement of a dense array of 250 nm diameter and 150 nm-high Si nanoscale discs effectively reduces the reflection from a Si wafer. Broadband antireflection exceeding the performance of a single layer ARC was also achieved by subsequently overcoating such particle arrays with a silicon nitride layer. In that work, the Authors convincingly argue that these large Si nanoparticles play a critical role as optical antennas, but no detailed design strategy was provided for the choice in particle size, shape, and spacing. A challenge toward this important goal was the relatively large physical size of the Si particles used in that study. Metamaterials based on such large, resonant scatterers cannot be described by zeroth-order effective medium theory,¹² which assumes that the electromagnetic fields do not exhibit spatial variations within the given materials.^{19–25} Whereas a second-order effective medium theory is more appropriate, it is also of great value to analyze whether the growing knowledge base in the field of Mie resonators can be leveraged to provide an alternative perspective of their operation. Recent theoretical work has attributed the antireflection to the destructive interference of light scattered by the particle-array and the reflection from the substrate.^{26,27} In this work, we take a

Received: July 6, 2018

Published: October 3, 2018

different starting point and develop an understanding for the operation of Mie-resonant ARCs by first analyzing the scattering properties of an individual Mie resonator placed on a Si substrate. We show how a judiciously designed Mie resonator can enable local antireflection and illustrate how ARCs based on optimized arrays of such Mie resonators can facilitate perfect antireflection at the wavelength where the resonator array displays its resonance. This indicates that the near-field optical coupling between resonators in the ARC is minimal, despite their close proximity. It also suggests that the resonators can enable antireflection in areas that are large compared to their geometric size. We then show how these two insights open the door to entirely new, multiresonant ARC designs capable of realizing antireflection at multiple wavelengths by having differently sized Mie resonators manage antireflection at different wavelengths. When optimized, such ARCs do not require a separate nitride layer to reach zero reflectivity across the solar spectrum.

For the construction of a Mie-resonance-centric model for ARCs constructed from semiconductor nanostructures, we start by investigating the scattering of a single Si nanowire (Si NW) placed on a Si substrate (see Figure 1). It is well-established that Si NWs support optical, Mie resonances at specific wavelengths that can be tuned with the NW size and geometrical shape.^{28–30} We first consider a 70 nm high NW with a square cross section. We choose this height to allow for an intuitive connection of the operation of a Mie resonance-based ARC to that of a conventional quarter-wavelength ARC based on silicon nitride. Figure 1a shows the measured backscattering spectrum for this NW taken in a darkfield configuration and with transverse electric (TE) polarized light (magnetic field oriented along the length of the NW). It shows a broad scattering resonance peaked at a wavelength of 470 nm that can be associated with a low-order Mie resonance that features a single antinode in the magnetic field in the NW core (Inset of Figure 1a). This wire serves as a magnetic dipole scatterer centered at about half the beam height. The spectrum closely matches the simulated backscattering spectrum (solid line). The inset shows a darkfield optical microscopy image of the NW with a predominantly blue color. Whereas in the darkfield configuration strong scattering is observed in the upward direction, in a bright field configuration, the NW scattering interferes with light that is backreflected from the Si surface. Depending on the relative phases, constructive or destructive interference can take place. Next, we will show that antireflection behavior can be achieved by optimizing the destructive interference case.

Without the Si NW, a polished Si wafer will reflect between ~30–45% of an incident light wave in the visible spectral range. One can analyze the properties of the reflected wave by performing a total-field scattered-field decomposition,³¹ where the total field is the sum of the incident and scattered fields. The left panel in Figure 1b shows the simulated scattered field for a 470 nm wavelength light beam that is normally incident on a smooth Si wafer. The flow lines of the Poynting vector (S_{scatt}) are overlaid on the field map and visualize the powerflow of the reflected light wave. The middle panel in Figure 1b shows a simulation of the scattered fields from the square Si NW upon illumination with TE light at the resonant wavelength of 470 nm. For this simulation, the incident fields are taken to be the standing wave fields in the presence of the bare Si substrate. With this choice of incident fields, the simulated scattered fields are those that result from the

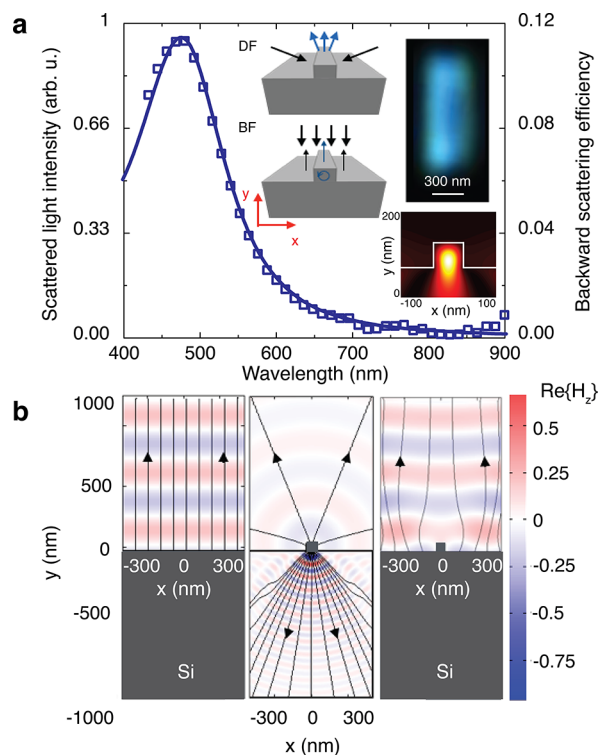


Figure 1. (a) Measured (dots, left-hand scale), simulated (continuous line, right-hand scale), and dark-field scattering spectrum for a 70 nm wide Si nanowire (Si NW) atop a Si wafer. The insets show schematics of the dark-field (DF) and bright-field (BF) configurations, a dark-field optical microscopy image of the Si NW, and a simulation of the magnetic field near a top-illuminated NW. (b) Total-field scatter-field simulations of the fields and powerflow lines along cross sections of our device structure. Illumination of the structure occurred at normal incidence at a wavelength of 470 nm, the peak of the backscattering spectrum shown in (a). The left panel shows the scatter-fields for a plane wave reflected from the Si substrate. The middle panel shows the scattered-field from the NW, calculated taking the standing wave above a planar Si substrate as the incident-field. The right panel shows the total-field for the top-illuminated NW.

placement of the Si NW on the substrate. The associated powerflow lines visualize how the NW on the substrate effectively scatters light toward the far-field with the density of the flow lines representing the magnitude of the local powerflow. As suggested by Spinelli et al.,¹⁹ the largest fraction of the scattered light is directed into the substrate. However, a substantial fraction of the scattered light (about 20% on resonance) is directed upward. This upward scattered light is essential for locally canceling the strong reflection from the Si substrate. By virtue of having the NW on resonance, the magnitude and phase of the scatter fields produced by the NW are such as to result in a perfect, local cancellation of the substrate reflection. This is seen in the simulation of the total field (right panel, Figure 1b), which shows lowered fields near the NW and no flow lines emerging from it.

In the preceding section, we demonstrated that a Mie resonance of a single Si NW can locally suppress reflection by destructive interference of its scattered wave with a reflected plane wave. However, the localized nature of the individual NW generates a scattered wave that decays in strength as it propagates radially outward and consequently the destructive interference does not persist in the farfield. To achieve

antireflection for the entire Si substrate, its surface will need to be covered with an array of Si NWs. In the following, we explore what happens for a periodic array of the square Si NWs as we increase the density while keeping the NW size fixed. The response of the nanowires is polarization-dependent. We are interested in the lowest resonant mode; therefore, we illuminate our structures with TE polarized light. Figure 2a shows a map of the simulated reflectivity as a function of the illumination wavelength and the array period. The period of 70 nm corresponds to a flat Si substrate, serving as a helpful reference. For larger periods, a broad and deep reflection minimum is found (blue region). The dashed white line identifies the spectral position of the reflection minimum for each periodicity. For the larger periods the spectral location of the reflection minimum is seen to be more-or-less independent of the period. In contrast, the reflection minimum redshifts substantially at shorter periods. The change in behavior takes place at a dividing line where the light wavelength in the high-index Si substrate matches the array period. Below this line, first-order diffracted beams are generated in the substrate. In this area of the map, the reflection minimum is spectrally located near the resonant wavelength of the individual NW. As the density of beams is increased, the minimum deepens. Above the line, no diffracted orders are generated and an effective medium description can be of value. In this regime, the array of 70 nm high NWs operates akin to a quarter wavelength antireflection coating whose effective index is controlled by the NW density. The dashed line shows the predicted wavelength at which the best antireflection can be observed using the first and second order effective medium approximation (EMA) for the effective optical properties.^{10–13,32–35} Within such approximations, the redshift simply results from the fact that the volume of Si increases with decreasing period and this increases the effective index of the layer.

To verify the behavior seen in Figure 1a, we fabricated arrays of Si NW on a Si substrate (see Methods) with periods ranging from 95–400 nm. Figure 2b shows the measured (symbols) and simulated (lines) reflection spectra for representative periodicities. At a 400 nm period, we observe a strong reflection minimum near the resonance frequency of the individual NWs (without neighbors). As predicted, the minimum deepens without a significant spectral shift until a case of “perfect” antireflection behavior occurs at a period of about 150 nm. For larger periods, the reflection minimum redshifts. Figure 2c shows the simulated (dashed red line) and measured (symbols) evolution of the reflectivity minimum versus the NW density. The left and right vertical dashed lines indicate the densities above which first-order diffracted beams can no longer be generated in the air and Si substrate, respectively. At the lowest densities, the reflectivity decreases from the reflectivity of the Si substrate as the NW density is increased. At such densities, it is impossible to realize effective antireflection as the diffracted-orders in the air cannot be canceled through destructive interference with the light reflected from the Si substrate. A kink in the reflectivity vs density curve is observed at the density where the higher-order diffracted beams in the air are precluded. As the density is further increased, the reflectivity initially decreases linearly with increasing NW density because the number of NWs causing local antireflection increases linearly. The solid gray line represents the best linear fit to the simulated reflectivity in this regime. The magnitude of its slope suggest that each NW

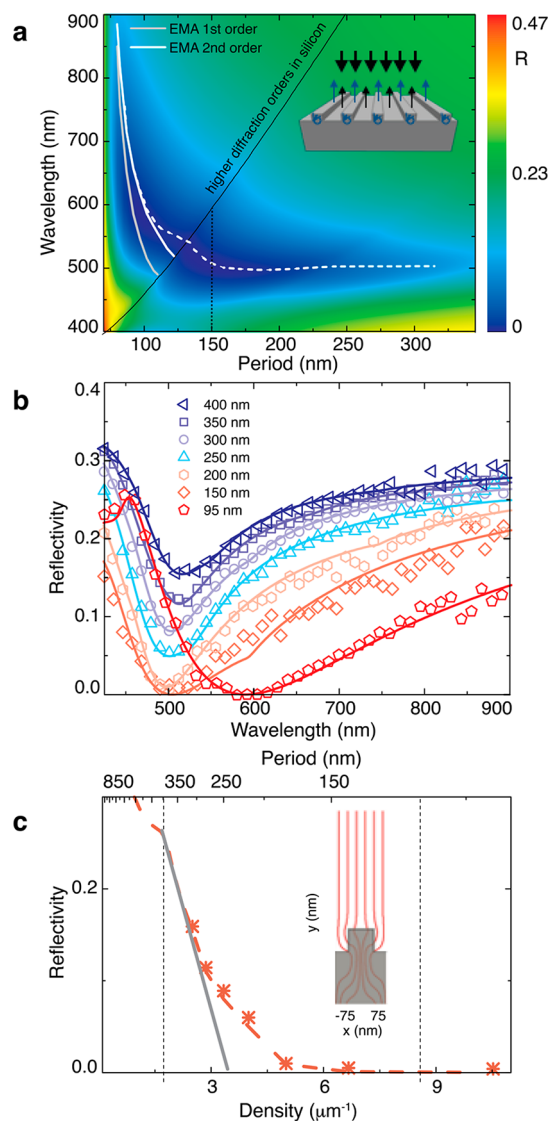


Figure 2. (a) Simulated reflectivity map for Mie resonant ARCs (inset) as functions of the illumination wavelength and array period. Light is TE polarized (the magnetic field is oriented along the length of the NW). The dashed white line shows the minimum points on the map. The continuous dark gray and the white lines are the expected minimum positions according to first-order and second-order effective medium approximations, respectively. The solid black line shows where the first-order diffraction channels open in Si substrate and we highlight the period of 150 nm near which the ARC operation changes from a nonresonant to a Mie-resonant metamaterial regime. (b) Simulated and measured reflection spectra for different array periodicities. (c) Simulated (dashed line) and measured (dots) values of the minimum reflectivity point in the reflection spectrum as a function of the array density (periodicity). The continuous line is the best linear fit of the data for smaller values of density. We highlight (gray dashed lines) the density values at which higher diffraction channels open in the air and Si substrate. Inset: Power flow lines associated for the total-field calculated for a 150 nm period NW array.

has an effective transmission cross section for redirecting light into the substrate that is about twice the physical width of the NW. The changes in the antireflection with increasing density become less rapid at higher densities as the NWs start to interact optically. This results from optical interference of the coherently driven NWs, which increases in importance as the radiation patterns of the NWs start overlapping (i.e., radiating

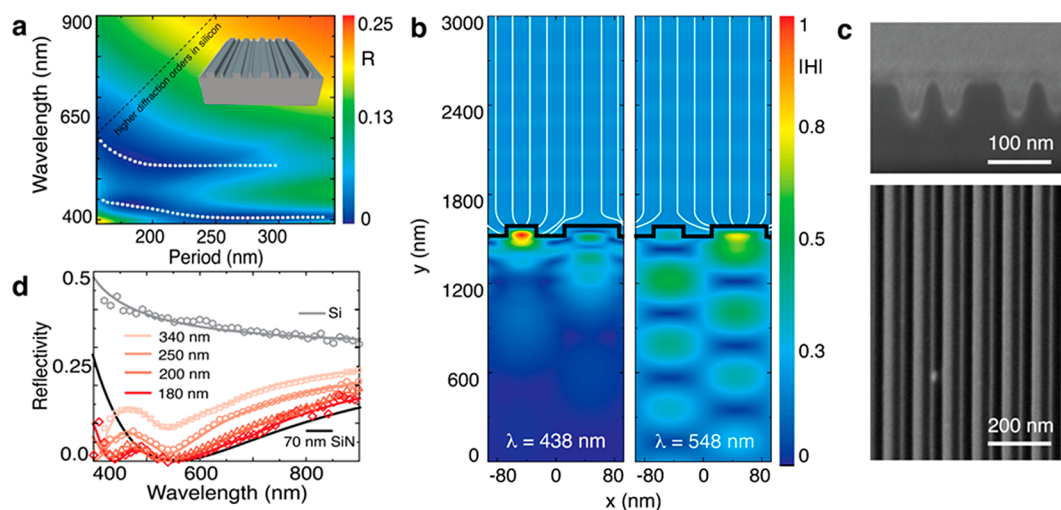


Figure 3. (a) Reflectivity map of a grating with 40 and 80 nm wide NWs interlaced (see inset) as functions of the two-NW unit cell period and illumination wavelength. Dashed lines depict the spectral locations of the reflectivity minimums associated with the resonances of the two NWs. (b) Map of the magnetic field magnitude along a cross section of the device structure at illumination wavelengths of 438 nm (left) and 548 nm (right). The flow of light into the patterned Si substrate is also shown by the flowlines of the Poynting vector (white). (c) Cross-section (top) and top-view (bottom) SEM images of the fabricated arrays with a 180 nm period. (d) Simulated (continuous lines) and measured (dots) reflection spectra of arrays with period ranging from 180 and 340 nm. Reflectivity from a bare Si wafer (gray) and a Si wafer (black) with a 70 nm thick Si₃N₄ ARC are reported for reference. Illumination is always TE-polarized.

into the same optical modes). At a density of $\sim 6.7/\mu\text{m}$ (period around 150 nm) the reflectivity reaches a zero value. The inset to Figure 2c shows the corresponding simulated powerflow lines for one unit cell. It shows that the condition for perfect antireflection is reached when the optical transmission cross section becomes equal to the period.

The antireflection behavior can also be understood physically by analyzing the possible way the light interacts with the nanostructured ARC. For NW densities at which the generation of the diffractive orders in the air is prevented, the backscattered light can only follow two distinct pathways. One pathway is the direct reflection from the Si substrate and the other is the resonant pathway through the NW array. With a properly tuned NW size and density, destructive interference of the light following these pathways occurs and gives rise to perfect antireflection. It is important to realize that a complete suppression of the reflection can be attained while the generation of diffracted orders in the Si substrate is allowed. This indicates that these ARCs can also offer a beneficial degree of light trapping/redirection of the incident light. When the density is increased further to periods below 150 nm, the minimum reflectivity remains low. However, the manner in which the ARC operates changes for two reasons. First, the spacing between the NWs at these high densities becomes sufficiently small that their near-fields start to overlap and the resonant behavior is less evident. Second, the possibility to generate diffracted orders in the Si substrate is removed. As a result, we enter the regime in which the effective medium approximation is effective at predicting the antireflection behavior. Here, the spectral location of the reflection minimum redshifts with increasing NW density due to the increase in effective index. It is noted that the antireflection behavior in most of Figure 2a, can be explained quite well using either a Mie resonator perspective at low NW density, and quite well using an EMA picture at high NW density. For a quarter-wavelength ARC these different operating regimes more-or-less smoothly transition into each other, facilitating a valuable

connection between conventional homogeneous ARC and Mie-resonant ARCs.

Figure 2 highlights that Mie-resonant ARCs operate in a very different way at low densities than conventional ARCs based on deep-subwavelength or densely spaced nanostructures. In the Mie-resonant regime, the spectral antireflection properties are largely controlled by the resonant properties of the high-index Mie resonators rather than the effective optical properties (complex refractive index) of a layer. The ability to determine the spectral location of a reflection minimum by manipulating the Mie resonances prompts the intriguing question whether antireflection behavior can be achieved at multiple wavelengths using differently sized or shaped resonators. As the scattering cross sections can exceed the geometrical cross section of a Mie resonator, it seems possible that different resonators can be placed on the same surface to manage the antireflection of light at different wavelengths.

In Figure 3 we analyze the reflection properties of an ARC that features two differently sized NW in a periodically repeated unit cell, as illustrated in the inset. We alternate NWs whose widths are 40 and 80 nm, while keeping the NW height at the original 70 nm. Structures are illuminated with TE-polarized light. In Figure 3a we show a color map the simulated reflectivity versus period and illumination wavelength. The map shows two distinct regions in which a low reflectivity is displayed (dark blue). One low reflection region occurs at shorter and one at longer wavelengths than the reflection minimum that was observed for the 70 nm wide beam (at 500 nm). To identify what resonances these features can be associated with, we analyze cross sectional field maps of the NW array for the periodicity of 185 nm where the lowest overall reflectivity is achieved (see Figure 3b). The map created at the shorter-wavelength reflectivity minimum ($\lambda = 438$ nm), we can see that light strongly interacts with the narrower resonator. At the longer-wavelength minimum ($\lambda = 548$ nm), the highest fields are seen in the wider NW. This suggests that the antireflection behavior at the different wavelengths is primarily managed by one of the NWs. We

also note that the wavefront in the substrate is affected by the presence of the nanostructures. While for traditional ARC, light propagates in the substrates as a plane wave, here we observe diffraction nodes and antinodes. For some applications this is a problem, while for others it can be an advantage. We believe this could be an advantage for thin film solar cells or solar cells employing a new device architecture designed to take advantage of light trapping. For AR coatings in glass, the redirected light from metasurfaces can also be used for a spectropolarimetric analysis of incident light. Of course, in vision and imaging applications the diffracted orders would need to be managed (suppressed or redirected outside of a field of view).³⁶

To experimentally verify the lowered reflectivity of a doubly resonant ARC, we fabricated the arrays with different unit cell periods. Figure 3c shows cross-sectional and top-view scanning electron microscopy (SEM) images of one of the fabricated arrays with a 180 nm period. Figure 3d shows the simulated and measured reflection spectra for several arrays with periods in the range from 180 to 340 nm. Reflection from a flat Si substrate is also measured for reference. Good agreement between experiment and simulations is obtained.

We again observe that the reflectivity decreases as the NW density increases, but now this occurs near the two wavelengths where the differently sized NWs are resonant. We achieve near-zero reflectivity at these wavelengths for a period of 180 nm (red curve). In this example, we designed the AR coating to reach low reflectivity near the peak of the solar spectrum. As a benchmark, we also show the simulated reflectivity from a Si wafer coated with a standard 70 nm thick silicon nitride layer. The metamaterial coatings provide a second reflectivity minimum near 440 nm that is not seen for the single-layer ARC. This is an area where Si strongly absorbs and the ARC would thus provide higher performance for solar cells that aim to harvest as much of the solar spectrum as possible.

So far, we have discussed the optical properties of one-dimensional (1D) Si NWs. However, in some applications, a polarization independent response is desired. We can use the same design strategy and extend it to 3D optically resonant nanoparticles. Figure 4a shows the simulated and measured reflection spectra for optimized samples that feature either one size of nanopillars or two distinct sizes. Top-view SEMs of these samples are provided as insets. Whereas the single-sized ARC provides a single minimum in the reflectivity in the visible range, the dual-sized ARC features two distinct minima. The left panel in Figure 4b shows the field distribution in a unit cell of the single-sized ARC when it is illuminated at normal incidence at a wavelength corresponding to the reflectivity minimum ($\lambda = 560$ nm). The middle and right panels show how light predominantly resonates in the narrow/wide pillar, depending on the wavelength. This confirms that Mie resonances play an equally important role in managing the light and antireflection behavior in these 3D nanostructures.

To evaluate the performance of low-density Mie-resonant ARCs for possible application in solar or other applications that require broadband antireflection, we compare the average reflection in the visible spectrum (400–800 nm) between these metasurfaces and a conventional quarter-wavelength silicon nitride layer. The monomodal pillar array exhibits an average reflectivity of 7%, consistent with the traditional silicon nitride ARC. The dual-sized pillar-array significantly outper-

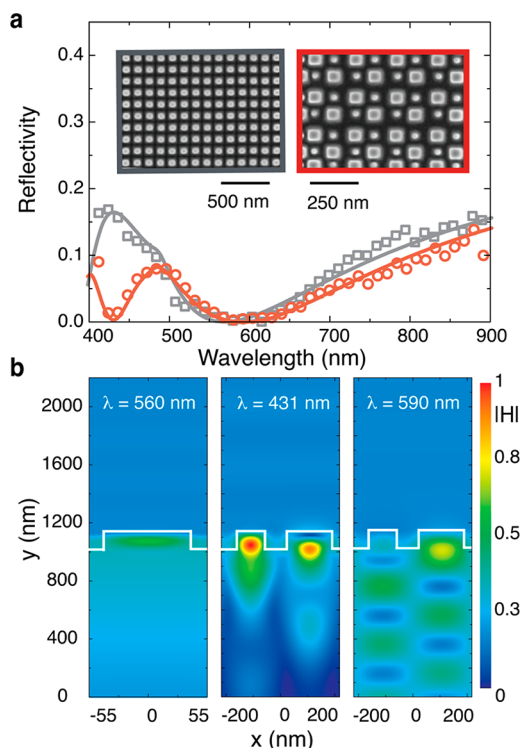


Figure 4. (a) Calculated (continuous lines) and measured (dots) reflection spectra of a Si wafer patterned with a single-sized (gray) and dual-sized (red) array of 3D pillars. (Inset) Top-view SEM images of the fabricated samples. Pillars in the single-sized ARC are 70 nm high and 80 nm in diameter and spaced by a period of 110 nm. In the dual-sized ARC, the Si pillars thickness is fixed at 75 nm, while the pillar diameters are 50 and 95 nm, respectively. In this case, unit-cell period is 215 nm. (b) Map of the magnitude of the magnetic field along a cross section of the device structures. Field is shown at 560 nm (left) for the monomodal array; 430 (middle) and 590 nm (right) for the dual-sized array.

forms the continuous layer with a spectrally averaged reflectivity as low as 4%, with a large transmission boost in the blue part of the spectrum.

In conclusion, we have demonstrated that Mie resonators can achieve effective local antireflection by canceling the reflected light from the substrate through destructive interference. In a sufficiently dense array, the antireflection properties are well-described by effective medium theory. However, at lower densities the antireflection properties are controlled by the optical resonances of the Mie resonators and the minimum reflectivity is achieved near their resonance frequency. With the use of differently sized resonators multiresonant ARCs can be realized that outperform traditional antireflection coatings and achieve near-unity transmission efficiency over a very broad spectral range. A thin electrical surface-passivation layer, if needed, does not alter this concept. The presented concepts can be applied to different frequency regimes or to include a plurality of differently sized/shaped resonators. Moreover, we used silicon for its wide use in the solar and microelectronics industries. These results can be easily extended to any other material, especially high refractive index materials, after a careful optimization of the size and periodicity of the nanostructures given the wavelength range of interest.

METHODS

The Si nanowire arrays in this study are fabricated on a Si wafer by focused ion beam (FEI Helios NanoLab 600i DualBeam FIB/SEM). We obtained cross-sectional SEM images after in situ covering the milled sample with a thick sacrificial layer of Pt in order to increase image contrast. Measurements of the reflected power are made using a confocal optical microscope (Nikon C1) coupled to a CCD camera (Acton Pixis 1024, Princeton Instrument) and spectrometer (Acton SP2300i, Princeton Instruments). The optical image is taken with the CCD camera after a color calibration. The calculation of the reflection map and reflection spectra is performed based on the finite-difference time-domain (FDTD) method (Lumerical Solutions Inc.) and using the refractive index values for Si reported in.³⁷ In Figure 1, we investigate the effect of a single nanowire on top of the semi-infinite Si wafer. Simulations are conducted using a total-field scattered-field light source and perfectly matched layer boundary conditions in all directions. For the simulations shown in Figures 2, 3, and 4, we assume periodic structures (periodic boundary conditions in the x -direction, perfectly matched layer in the y -direction) under illumination with a plane wave. The reflectivity values in Figure 2a are evaluated according to the first order and second order effective medium theory.

AUTHOR INFORMATION

Corresponding Author

*E-mail: brongersma@stanford.edu.

ORCID

Emanuele F. Pecora: 0000-0003-2467-5486

Andrea Cordaro: 0000-0003-3000-7943

Mark L. Brongersma: 0000-0003-1777-8970

Author Contributions

E.F.P. and A.C. conceived the original ideas for this work. E.F.P., A.C., P.G.K., and M.L.B. designed the experiments. E.F.P. prepared the samples and carried out the experiments. E.F.P. and A.C. conducted the simulations and theoretical calculations. All authors analyzed and discussed the results and were involved in writing the manuscript.

Notes

The authors declare no competing financial interest.

ACKNOWLEDGMENTS

Part of this work has been performed at the Stanford Nano Shared Facilities and was funded by a gift from ENEL Green Power and the Bay Area Photovoltaics Consortium. The data that support the plots within this paper and other findings of this study are available from the corresponding author upon reasonable request.

REFERENCES

- (1) Rayleigh, L. On Reflection of Vibrations at the Confines of Two Media between which the Transition is Gradual. *Ann. Phys.* **1879**, *1*, 51–56.
- (2) Stephens, R. B.; Cody, G. D. Optical reflectance and transmission of a textured surface. *Thin Solid Films* **1977**, *45*, 19–29.
- (3) Krč, J.; Smole, F.; Topič, M. Potential of Light Trapping in Microcrystalline Silicon Solar Cells with Textured Substrates. *Prog. Photovoltaics* **2003**, *11*, 429–436.
- (4) Koynov, S.; et al. Black nonreflecting silicon surfaces for solar cells. *Appl. Phys. Lett.* **2006**, *88*, 203107.
- (5) Yablonovitch, E.; Cody, G. D. Intensity Enhancement in Textured Optical Sheets for Solar-Cells. *IEEE Trans. Electron Devices* **1982**, *29*, 300–305.
- (6) Her, T. H.; Finlay, R. J.; Wu, C.; Deliwala, S.; Mazur, E. Microstructuring of silicon with femtosecond laser pulses. *Appl. Phys. Lett.* **1998**, *73*, 1673–1675.
- (7) Sánchez-Gil, J. a.; Nieto-Vesperinas, M. Light scattering from random rough dielectric surfaces. *J. Opt. Soc. Am. A* **1991**, *8*, 1270.
- (8) Branz, H. M. Nanostructured black silicon and the optical reflectance of graded-density surfaces. *Appl. Phys. Lett.* **2009**, *94*, 231121.
- (9) Wang, K. X.; Yu, Z.; Liu, V.; Cui, Y.; Fan, S. Absorption enhancement in ultrathin crystalline silicon solar cells with antireflection and light-trapping nanocone gratings. *Nano Lett.* **2012**, *12*, 1616–1619.
- (10) Raguin, D. H.; Morris, G. M. Antireflection structured surfaces for the infrared spectral region. *Appl. Opt.* **1993**, *32*, 1154.
- (11) Smith, R. E.; Warren, M. E.; Wendt, J. R.; Vawter, G. Polarization-sensitive subwavelength antireflection surfaces on a semiconductor for 975 nm. *Opt. Lett.* **1996**, *21*, 1201–3.
- (12) Lalanne, P.; Hutley, M. The optical properties of artificial media structured at a subwavelength scale. *Encyclopedia of Optical Engineering* **2003**, 62–71.
- (13) Catchpole, K. R.; Polman, A. Design principles for particle plasmon enhanced solar cells. *Appl. Phys. Lett.* **2008**, *93*, 191113.
- (14) Gaylord, T. K.; Baird, W. E.; Moharam, M. G. Zero-reflectivity high spatial-frequency rectangular-groove dielectric surface-relief gratings. *Appl. Opt.* **1986**, *25*, 4562–4567.
- (15) Ono, Y.; Kimura, Y.; Ohta, Y.; Nishida, N. Antireflection effect in ultrahigh spatial-frequency holographic relief gratings. *Appl. Opt.* **1987**, *26*, 1142–1146.
- (16) Motamedi, M. E.; Southwell, W. H.; Gunning, W. J. Antireflection surfaces in silicon using binary optics technology. *Appl. Opt.* **1992**, *31*, 4371–4376.
- (17) Smith, R. E.; Warren, M. E.; Wendt, J. R.; Vawter, G. a. Polarization-sensitive subwavelength antireflection surfaces on a semiconductor for 975 nm. *Opt. Lett.* **1996**, *21*, 1201–3.
- (18) Vasudev, A. P.; Schuller, J. A.; Brongersma, M. L. Nanophotonic light trapping with patterned transparent conductive oxides. *Opt. Express* **2012**, *20*, A385.
- (19) Spinelli, P.; Verschuuren, M.; Polman, A. Broadband omnidirectional antireflection coating based on subwavelength surface Mie resonators. *Nat. Commun.* **2012**, *3*, 692.
- (20) Pala, R. A.; Butun, S.; Aydin, K.; Atwater, H. A. Omnidirectional and broadband absorption enhancement from trapezoidal Mie resonators in semiconductor metasurfaces. *Sci. Rep.* **2016**, *6*, 31451.
- (21) Baryshnikova, K. V.; Petrov, M. I.; Babicheva, V. E.; Belov, P. A. Plasmonic and silicon spherical nanoparticle antireflective coatings. *Sci. Rep.* **2016**, *6*, 22136.
- (22) Wang, Z. Y.; et al. Broadband optical absorption by tunable Mie resonances in silicon nanocone arrays. *Sci. Rep.* **2015**, *5*, 7810.
- (23) Kuznetsov, A. I.; Miroshnichenko, A. E.; Brongersma, M. L.; Kivshar, Y. S.; Lukyanchuk, B. Optically resonant dielectric nanostructures. *Science* **2016**, *354*, 2472–2472.
- (24) Campbell, P.; Green, M. A. Light trapping properties of pyramidally textured surfaces. *J. Appl. Phys.* **1987**, *62*, 243–249.
- (25) Van De Groep, J.; Spinelli, P.; Polman, A. Single-Step Soft-Imprinted Large-Area Nanopatterned Antireflection Coating. *Nano Lett.* **2015**, *15*, 4223–4228.
- (26) Baryshnikova, K. V.; Petrov, M. I.; Babicheva, V. E.; Belov, P. A. Plasmonic and silicon spherical nanoparticle antireflective coatings. *Sci. Rep.* **2016**, *6*, 22136.
- (27) Wang, K. X.; Yu, Z.; Sandhu, S.; Liu, V.; Fan, S. Condition for perfect antireflection by optical resonance at material interface. *Optica* **2014**, *1*, 388.
- (28) Brongersma, M. L.; Cui, Y.; Fan, S. Light management for photovoltaics using high-index nanostructures. *Nat. Mater.* **2014**, *13*, 451–60.

- (29) Wang, K. X.; Yu, Z.; Sandhu, S.; Liu, V.; Fan, S. Condition for perfect antireflection by optical resonance at material interface. *Optica* **2014**, *1*, 41–47.
- (30) Yu, Z.; Raman, A.; Fan, S. Nanophotonic light-trapping theory for solar cells. *Appl. Phys. A: Mater. Sci. Process.* **2011**, *105*, 329–339.
- (31) Taflove, A.; Hagness, S. C. *Computational Electrodynamics: The Finite-Difference Time-Domain Method*; Artech House: Boston, MA, 2000.
- (32) Bohren, C. F.; Huffman, D. R. *Absorption and Scattering of Light by Small Particles*; John Wiley & Sons, 1983; Vol. 541, p 1.
- (33) Cao, L.; et al. Engineering light absorption in semiconductor nanowire devices. *Nat. Mater.* **2009**, *8*, 643–7.
- (34) Cao, L.; Fan, P.; Barnard, E. S.; Brown, A. M.; Brongersma, M. L. Tuning the color of silicon nanostructures. *Nano Lett.* **2010**, *10*, 2649–2654.
- (35) Wenshan, C.; Shalaev, V. *Optical Metamaterials: Fundamentals and Applications*; Springer, 2009; Vol. 2, p 1.
- (36) Li, Q.; Dong, F.; Wang, B.; Chu, W.; Gong, Q.; Brongersma, M. L.; Li, Y. Free-Space Optical Beam Tapping with an All-Silica Metasurface. *ACS Photonics* **2017**, *4*, 2544–2549.
- (37) Palik, E. *Handbook of Optical Constants of Solids*; Elsevier, 1998.